High-Efficiency Diagnosis of Antenna Radiation Characteristics Based on Scanning Optic-Induced Plasma Scattering Technology

Liao Ma⬦, Ning Leng⬦, Ming Jin, *Member, IEEE*, and Ming Bai⬦, *Member, IEEE*

Abstract— **This article presents an innovative quasi-real-time antenna near-field diagnosis method, by scanning a laser-induced plasma on a silicon wafer and imaging the field with the synchronously produced scattered signals. Several approaches have been devised to adapt to the antenna diagnosis scenarios. By using the multilayer matching approach, the issue of multiple reflection disturbance between the aperture and silicon wafer is avoided, especially for large aperture antennae at high frequencies. The accuracy of near-field distribution is improved, and far-field patterns can be transformed directly. The experimental results of a Ka-band 20 dB standard antenna agree well with the simulation results. Diagnosis of radiation states in the reactive near-field region is demonstrated, and the resonate modes of a 2.4 GHz Wi-Fi patch antenna at different frequencies are clearly observed. The experiments of a TM_{01} mode antenna verify the full polarization diagnosis ability of the method, and the linear polarization component is measured with the help of a polarization grid. The demonstrated diagnosis method has the advantages of high efficiency, ultraclose measurement distance, and superresolution and provides a highly promising and widely available method for antenna diagnosis.**

Index Terms— **Antenna measurements, microwave photonic, modulated scattering technology, near-fields, photoconductivity, plasmas.**

I. INTRODUCTION

NEAR-FIELD measurement is a widely used standard antenna measurement technology with the advantages of intuitiveness and convenience [1], [2], [3]. The rich information can be obtained by scanning a probe to diagnose the antenna characteristics of near-field, far-field, polarization, and radiation mode. The most common probes used for near-field scanning are open-ended waveguides [3], antennas, and scatters [4], [5]. Different kinds of probes based on electrooptic and magnetooptic effects are used for high-resolution or high-sensitivity detection of electromagnetic fields. An electrooptic probe based on a crystal of GaAs [6] is used for detecting terahertz electromagnetic waves. Nanoscale diamond nitrogen-vacancy center probes are designed for quantum magnetic field detection and realize nanoscale resolution scanning [7], [8]. A Rydberg atom-based probe can detect electric fields with high sensitivity [9], [10]. However, mechanical scanning is necessary for these probes to get the distribution of the field. In this case, measurement accuracy and efficiency become conflicting issues. Various efficient electromagnetic sampling algorithms, such as sparse sampling [11], [12], [13], [14], compressed sensing [15], [16], [17], [18], adaptive sampling [19], and nonredundant sampling [20], [21] have been proposed to improve the efficiency of the probe scanning method by reducing the number of sampling points. Fixed probe arrays [5], [22], [23], [24] have also been introduced to improve efficiency, but the resolution is limited by the size of the fixed probe. Complex and expensive array systems are only in exchange for efficiency increases under special measurement conditions, such as limited frequencies or limited imaging areas. High-speed CCD camera is used to realize real-time electromagnetic field imaging by detecting the variation of the optic signals varies through the diamond of ZnTe [25] and nitrogen-vacancy center [26]. Limited by the size of CCD, the imaging area of these methods is only tens of millimeters at most, which cannot meet the needs of antenna near-field measurement. Efficient and practical near-field measurement methods have been an intractable dream for a long time.

Based on our previous work [27], we invented scanning optic-induced plasma scattering (SOPS) technology to realize the near real-time imaging of the electromagnetic field. Due to the photoconductive effect, the semiconductor material is excited out of the electron–hole pairs and forms a plasma region [28], [29], [30], [31], [32] under the irradiation of a near-infrared laser. The conductivity changes in the plasma region are utilized as a massless scattering probe to image the electromagnetic field with an efficient laser scanning scheme. This new electromagnetic imaging technology combines the advantages of ultrafast speed, superresolution, ultrawideband response, and low complexity.

Therefore, SOPS technology has the potential to offer an efficient method for diagnosing the radiation characteristics of an antenna under test (AUT). To achieve this goal, there are still some issues that need to be resolved. It is found that the

reflectivity of the wafer increases with frequency. For example, with a 0.3 mm-thick silicon wafer, the reflectivity of the wafer is higher than -10 dB when the frequency of the incident wave is higher than 10 GHz. Then, the multireflected waves between the wafer and the aperture structure of the antenna may build up, which may cause a noticeable disturbance in the imaging results, however depending on the size of the antenna. To improve the accuracy for different types of AUTs, the multiple reflection disturbance shall be eliminated as much as possible. Furthermore, far-field and polarization characteristics are also often of interest for antenna diagnostics, as well as the radiation states of the antennas. It would be of great value if this efficient technology should be expanded to a variety of diagnostic scenarios.

In this article, a high-efficiency antenna diagnosis method is realized based on SOPS technology. More accurate near-field distributions of antenna radiation are obtained after solving the issue of multiple reflection disturbance by a multilayer matching approach, and systematic diagnoses of antenna characteristics are carried out, including far-field patterns, radiation states in the reactive near-field region, and polarization characteristics. Amplitude and phase distributions of the antenna in the radiating and reactive near-field region are measured effectively in seconds and further used to diagnose the characteristics of the far-field pattern and radiation states of the antenna. The full polarization characteristics of a TM_{01} mode antenna are measured directly, and linear polarization components are obtained assisted by a polarization grid. With these improvements, the SOPS technology is systematically developed and adapted for antenna radiation characteristics diagnosis and is experimentally proven to be an innovative method for high-efficiency antenna diagnosis. This demonstrated antenna diagnosis method will greatly benefit the research and application of antenna measurements.

II. PRINCIPLE OF DIAGNOSIS

A. Scanning Plasma Scattering Technology

SOPS technology was invented as a basic technology for fast imaging of electromagnetic fields [27]. The core idea of the technology is to use a massless scattering "probe" to measure the electromagnetic field, replacing the probe transport mechanism with an ultrafast scanning laser. The resolution of the imaging is affected by the arrangement of the plasma, which mainly depends on the diameter of the laser beam [33] and can be significantly smaller than the aperture of a conventional probe. In microwave bands, superresolution and ultrafast imaging speed can be realized at the same time [27].

The data-processing procedure of imaging electromagnetic field from the scattered signals can refer to the modulated scattering technique [34], [35], [36], [37], [38], [39]. According to the reciprocity principle, the electromagnetic field to be measured, recorded as E_{AUT}, is proportional to the square of the variation of the backscattered signal ΔS_{11} [27]

$$E_{AUT} = C\sqrt{\Delta S_{11}} \qquad (1)$$

where C is approximately a constant at different laser scanning points, which is influenced by material properties and
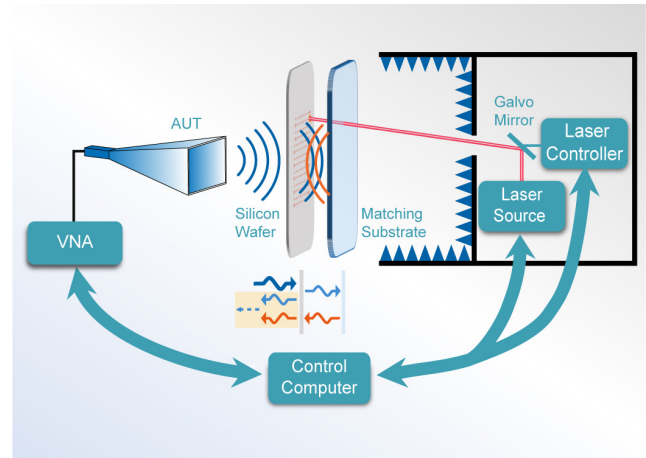

Fig. 1. Improved scheme of the high-efficiency antenna diagnosis method. A plasma spot is excited on the silicon wafer with the illumination of a near-infrared laser beam. The scattered electromagnetic wave at the illuminated point is recorded by the VNA receiver. With the synchronized control of VNA, the laser source, and the controller by computer, the distribution of the electromagnetic field in an area on the wafer can be efficiently obtained with laser scanning. The scheme is improved with the multilayer matching approach, which is applied to reduce the multiple reflection disturbance between the antenna aperture and the wafer, using an optically transparent sheet.

illumination conditions. ΔS_{11} can be simply obtained from the difference of the back transferred signal S_{11} measured by VNA with or without the illumination. As the value of C does not affect the relative distribution of the electromagnetic field, using this elegant mathematical relation, the relative value of E_{AUT} can be recorded in the vector form at each illuminated point and efficiently obtain the electric field distribution of an area with the help of laser scanning.

B. Design of Diagnosis for Antenna Radiation Characteristics

The SOPS technology provides a real-time technology to image electromagnetic fields, combining various advantages [27]. Applying this technique to antenna diagnosis is so attractive, but it still faces a few issues. The most apparent one is the reflection effect from the wafer, especially when the antenna aperture is placed at a near distance.

The relative permittivity of the silicon wafer is 11.5. The thickness of the silicon wafer is 0.3 mm, which is much thinner than the wavelength in the microwave band. The reflectivity of the single wafer increases with frequency. The reflectivity is less than -15 dB when the frequency is below 5 GHz, and its impact on the original field is small enough to be negligible.

As the frequency gets higher, the reflectivity of the wafer increases, and disturbance caused by the multireflection waves between the antenna aperture and the wafer is found to be nonnegligible, especially for the large-aperture antenna. In this case, the measured E_{AUT} consists of the field to be measured and the disturbance caused by the reflected field. To improve the accuracy for more types of AUTs, the multilayer matching approach is introduced to the scheme.

As shown in Fig. 1, the prototype mainly consists of a wafer, a laser source, a galvo mirror, and a laser controller.
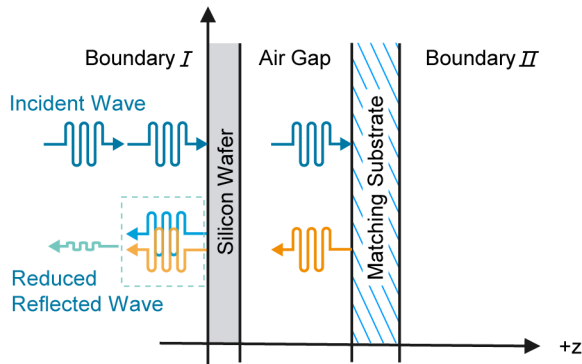
Fig. 2. Principle of multilayer matching.

All components can be integrated within a small box of $0.4 \times 0.3 \times 0.2$ m, and these components are easily purchased at low cost. This makes the prototype compact and economical. The AUT is connected to a VNA (Ceyear AV3672C modal, 10 MHz–43.5 GHz), which is used as a transceiver to build this monostatic measurement system. The laser (100 mw, 980 nm in wavelength) is controlled to scan the imaging area on a thin silicon wafer (P111 intrinsic type, 300 μm in thickness) with a galvo mirror system. The computer controls the VNA, the laser source, and a controller and synchronously records the backscattered signals from the VNA at each scanning point. With these scattered signals, the radiation field in the scanned area can be retrieved and mapped.

In general, the incident wave on the wafer consists of plane wave components in multiple directions. For directional antennas, which are suitable for the planar near-field scanning method [3], the major part of the beam can be assumed to consist of plane wave components approximately perpendicular to the wafer.

In this case, the planar multilayer matching approach is designed as follows. A three layers matching is designed as an example. The first layer is a thin silicon layer for inducing the plasma. A thin wafer can confine the plasma within a flake region, reducing the unpredictable scattering signals caused by the plasma diffusing along the thickness. The second layer is the air gap for adjusting the matching situation, and the third layer is a matching substrate. As shown in Fig. 2, it is assumed that most of the incident wave is perpendicular to the silicon wafer, and it will produce the reflected wave (light blue) and transmitted wave on the surface of the wafer. The transmitted wave passes through the silicon wafer and air gap and then produces the reflected wave (orange) on the surface of the matching substrate. This reflected wave is transmitted to the wafer surface through the air gap again. The phase of this reflected wave (light orange) can be adjusted to the opposite phase of the reflected wave (light blue) produced by the original incident wave by changing the distance of the air gap. In this case, the total reflectivity of the whole layers will reduce to the minimum, and the wafer can be considered to be matched by the matching substrate.

When plane waves normally incident into the multilayer medium in the $+z$-direction, the reflectivity on the boundary I can be easily calculated with the permittivity and thickness

TABLE I
PERMITTIVITY AND LASER TRANSMITTANCE OF SiO_2 DOPED WITH DIFFERENT METAL IONS

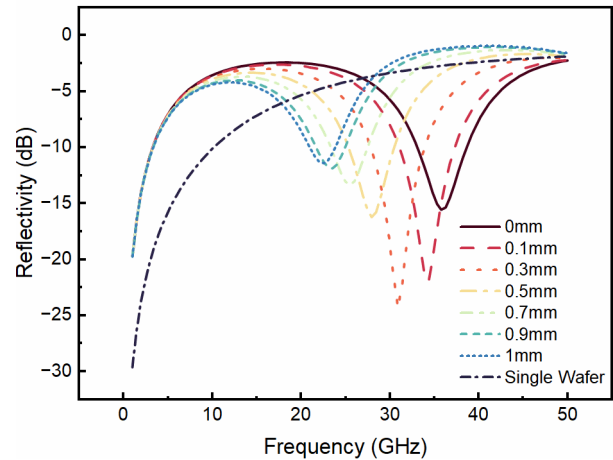| Materials	Permittivity	Laser transmittance(980nm)
SiO_2	3.65 - 0.015j	93.59%
Na_2O	7.175 − 0.323j	91.38%
Al_2O_3	6.8 - 0.258j	92.02%

Fig. 3. Simulated reflectivity results for a single 0.3 mm silicon wafer, and total reflectivity of the whole layers with a 1.1 mm Na_2O-doped glass matching substrate at different thicknesses of the air gaps.

of the three layers by the matching and propagation matrices [40]. By designing the permittivity and thickness of each layer, the minimum reflectivity at a given frequency can be obtained, and the matching condition is achieved at this frequency.

The matching substrate should have a high dielectric constant and a low loss to produce enough reflection for matching the waves reflected from the wafer. At the same time, it should have a high transmittance for the scanning laser at 980 nm. SiO_2 doped with metal ions is a good choice. The permittivity and laser transmittance of different metal doping are selected and tested, with results shown in Table I.

Na_2O- or Al_2O_3-doped glass has a higher relativity permittivity close to the silicon wafer and both can be chosen as the matching substrate. A sheet of Na_2O-doped glass with a thickness of 1.1 mm is selected as the matching substrate. Simulation results of total reflection for the whole layers with a different air gap of 0–1 mm are shown in Fig. 3.

As shown in Fig. 3, the whole reflectivity is reduced significantly at certain matching frequency points. Under this matching condition, the reflected wave from the wafer and the matching substrate can be considered to have a similar amplitude and inverse phase, and the total reflectivity gets smallest. The phase difference between the two reflection waves can be adjusted by the thickness of the air gap, as the length of the wave path changes. To maintain the matching condition, the matching frequency decreases with the increase of the air gap, and the total reflectivity curve shifts to the low-frequency direction. At these matching frequencies, the total reflected wave from the wafer is small enough, and
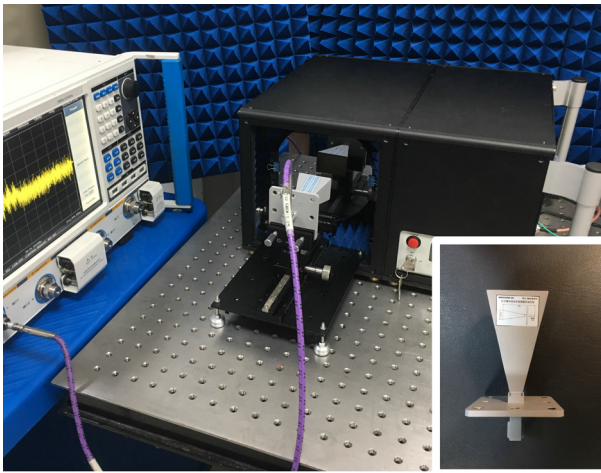
Fig. 4. Photograph of the experimental setup with the prototype.

the disturbance caused by the multireflection waves will be suppressed dramatically.

It is clear that the matched frequency points and reflection coefficient are influenced by the dielectric constant and the air layer thickness. Therefore, by adjusting the air gap, the matching frequency can be adjusted to the designed operating frequency of the antenna. Such that, it is convenient to adjust and achieve broadband matching. As the example shown in Fig. 3, the matching frequency can be adjusted from 24 to 35 GHz, covering almost the entire Ka-band, by changing the air gap from 0 to 1 mm. For different frequency bands, similar matching designs can be realized.

III. Diagnosis of Antenna Radiation Characteristics

A. Near-Field Distribution and Far-Field Pattern

We deliberately choose a Ka-band 20 dB standard gain antenna as the AUT, with a large aperture of 47×33 mm. The matching substrate is a sheet of Na_2O-doped glass with a thickness of 1.1 mm. The matching frequency is selected at 34.162 GHz by adjusting the air gap to 0.1 mm, according to the results of Fig. 3. The imaging area is 100×100 mm with 101×101 points. The experimental setup with the prototype is shown in Fig. 4.

The near-fields of the AUT at 30 mm from the aperture are measured with multilayer matching layers. The distance is in the radiating region of the antenna. The corresponding simulated field of the AUT and the measured results with the single wafer are also compared, as shown in Fig. 5.

Compared to results by a single wafer in Fig. 5(a), the results by multilayer matching in Fig. 5(b) are more consistent with the simulation results in Fig. 5(c), and clearly compared in the 1-D curves in Fig. 5(d) and (e). It is experimentally verified that the multilayer matching approach has been effective in suppressing multiple reflected waves.

At the same time, the signal-to-noise ratio (SNR) under the multilayer matching condition is also improved compared to the single-wafer condition. It is because the backscattering signals are more dominant when the reflection waves are much
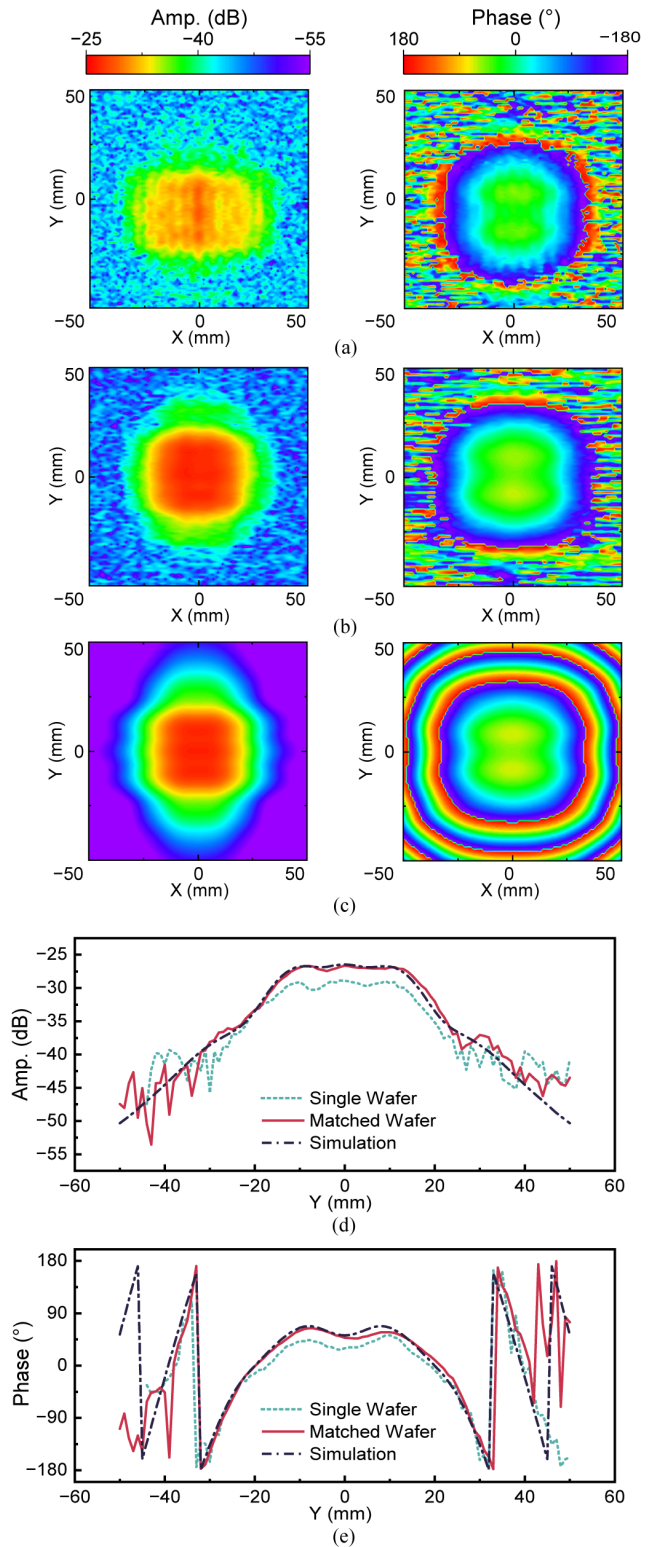

Fig. 5. Experimental results at 30 mm from the AUT aperture. (a) Measured results with the single wafer. (b) Measured results with multilayer matched wafer. (c) Simulated results of the AUT at the same distance. The 1-D (d) amplitude and (e) phase comparison curves when x is zero.

suppressed. With the multilayer matching method, the quality of the field imaging is improved significantly, especially for the large-aperture antenna.
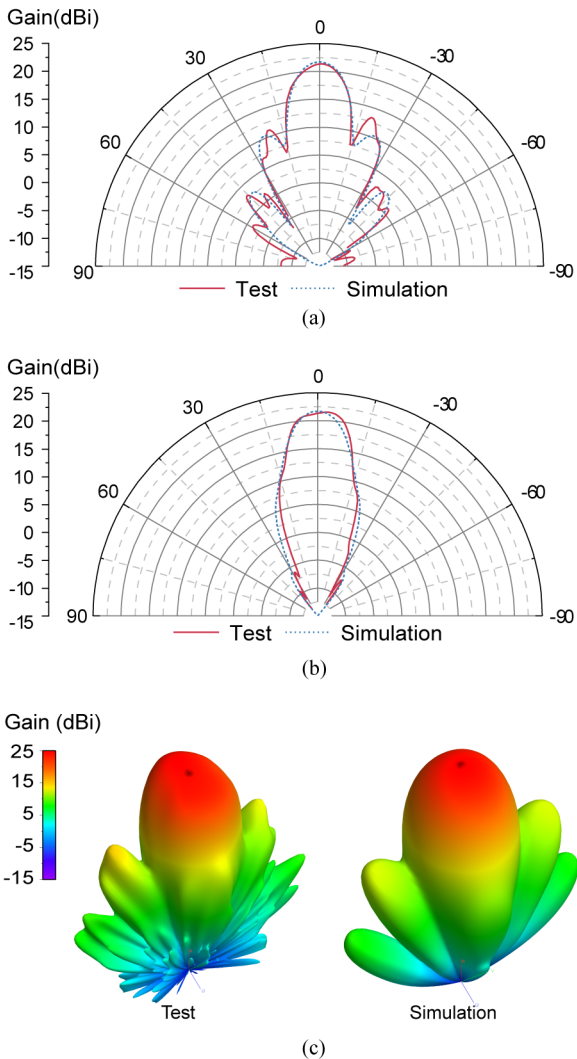
Fig. 6. Far-field results of the antenna. The far-field pattern of the AUT can be transformed from the results of the near-field in Fig. 5(b) and is compared with the simulated far-field pattern of the AUT. Polar coordinate far-field gain pattern comparison of (a) E-plane pattern cut and (b) H-plane pattern cut. (c) Three-dimensional far-field pattern comparison.
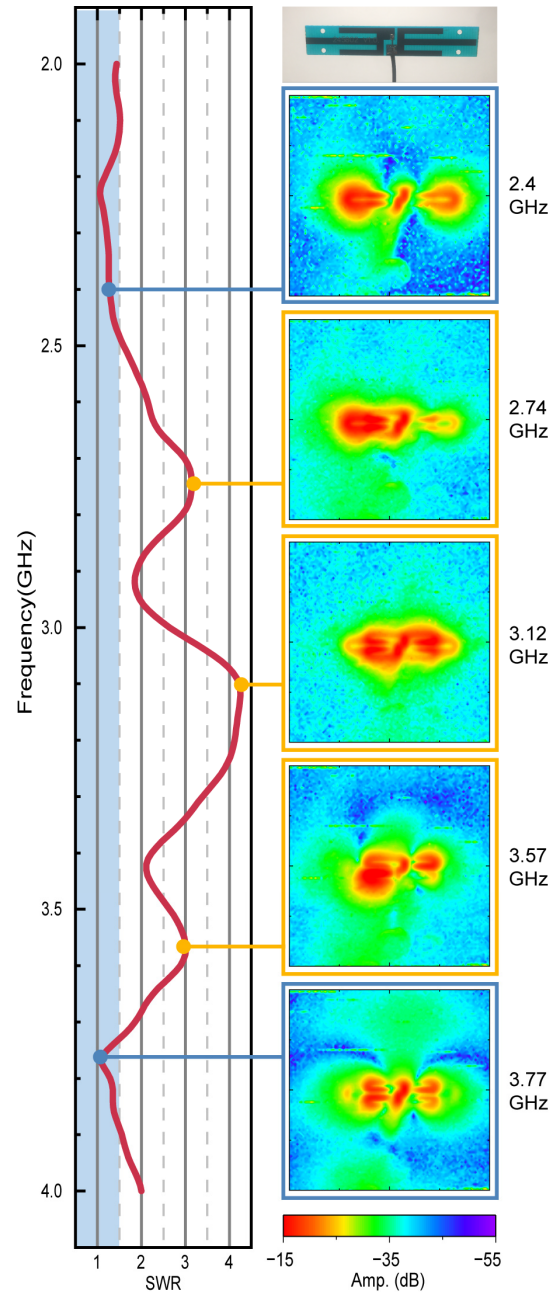

Fig. 7. Diagnosis of the patch antenna at the reactive near-field region with different frequencies. The left part is the standing wave ratio (SWR) curve of the AUT from 2 to 4 GHz, and the right part is the measured amplitude distributions at selected corresponding frequency points.

The far-field results of the antenna can be obtained by transforming from the near-field distributions, based on the basic algorithm of the field equivalence principle [40]. Parallel computing is used to accelerate the computing process, and the full far-field patterns can be obtained almost instantly. The gain of an antenna can be determined by the directivity and efficiency of the antenna [3]. For a lossless antenna like the one used in the experiment, which indicates the efficiency is close to one, the gain is the same as the directivity of the antenna. The transformed far-field gain patterns are shown in Fig. 6 and compared with the simulated patterns. Two results are agreed well in the mainlobe, and the measured maximum gain is very close to the simulated result.

The SNR of the current prototype limits the sensitivity of the imaging, resulting in the truncation of the energy in the near-field distribution. In Fig. 5(b) and (c), there are differences mainly in the area of the weak signals around the main beam, where the signals are less than −20 dB of the peak value.

Therefore, this truncation of the energy in the near-field causes notable differences in the sidelobe of the far-field pattern.

B. Radiation State Diagnosis in Reactive Near-Field Region

The method can be applied to diagnose the antenna at a close distance, including the reactive near-field region of the antenna. As a demonstration, a handy 2.4 GHz WiFi patch antenna is selected as the AUT, and the measured reactive near-field results are shown in Fig. 7. The reactive near-field of the patch antenna can be clearly observed from

the amplitude distributions in Fig. 7. This phenomenon in the reactive near-field region shows the radiation states of the patch antenna directly, which was previously difficult to measure and always relied on simulations.

More interesting results can be obtained from the distributions at different frequencies with different SWR states. At the designed operating frequency of 2.4 GHz, the SWR is lower than 1.5, the AUT works well, and the energy is symmetrically radiated as expected. The same phenomenon can be found in the distribution at 3.77 GHz. When SWR hits its peak over 3.1 at 2.74 and 3.57 GHz, the radiation of the antenna is asymmetrically concentrated on the left side, which will not have normal radiation efficiency. The asymmetrical distributions at these frequencies are caused by the special resonant state of the patch antenna, which is affected by the antenna structure, form of feed, solder joint matching condition, and so on. At 3.12 GHz, when SWR maximizes and exceeds 4, the patch structure edge can be seen under this special resonance condition. The energy is bound in the surface waves and does not show a radiating pattern.

Although the antenna works well at 2.4 and 3.77 GHz when SWR is below 1.5, the resonant modes are significantly different. Additionally, at frequencies of 2.74 and 3.12 GHz, the resonant modes are also different when SWR becomes worse. These distributions reveal that the patch antenna may have different characteristic mode patterns at similar transmission states. The method is demonstrated as an intuitive tool to diagnose the radiating behavior of antennas and would be helpful for antenna design and optimization with antenna characteristic modes technology [41], [42], [43], [44].

Furthermore, since the entire imaging area is 100×100 mm, the details of the structure shown in Fig. 7 are significantly smaller than the wavelength (125 mm at 2.4 GHz). These images give superresolution details for near-field analysis of the antenna.

C. Polarization Characteristics Diagnosis

In fact, the scattering of electromagnetic waves by optic-induced plasma is not polarization-selective, but contains the full polarization response of antenna radiation. As an example, the near-field radiation distribution of a Ka-band TM_{01} model antenna [45] is measured as shown in Fig. 8(a). The distribution shows a typical TM_{01} mode pattern with full polarization features, which usually cannot be obtained in a single measurement with linearly polarized probes. The polarization-insensitive measurement can be useful for the efficient diagnosis of antennas, such as circularly polarized antennas or multipolarized antennas.

Still, if a linearly polarized radiation field should be measured, a polarization grid can be used to get a specific linear polarization component. The linear polarization component of the AUT is easily obtained by placing a sheet of polarization grid in the corresponding direction between the antenna aperture and the silicon wafer. As a demonstration, the AUT in the horizontal, vertical, and tilted polarization states is measured by placing the polarization grid in the horizontal and vertical directions or in any desired direction,
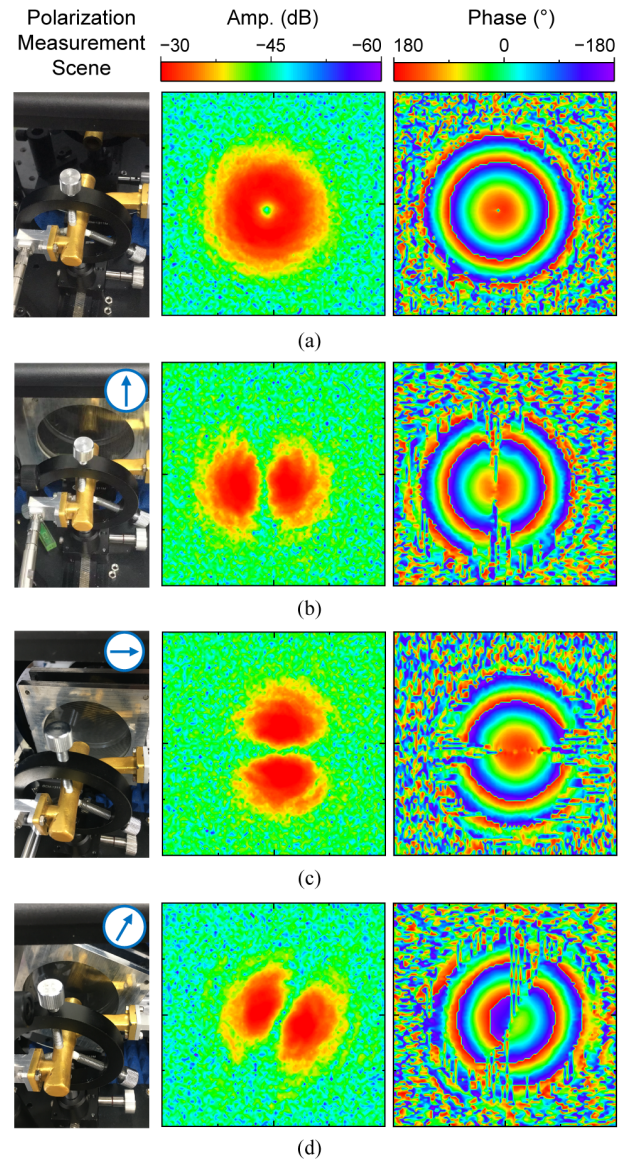

Fig. 8. Polarization measurement of a TM_{01} model antenna. (a) Full polarization results without the polarization grid. Linear polarization component measured with the polarization grid placed in (b) vertical, (c) horizontal, and (d) tilted conditions.

as shown in Fig. 8(b)–(d). It provides a very intuitive and efficient understanding of the radiation characteristics of this special multipolarized mode antenna. These results show the flexibility and adaptability of this technique to polarization diagnosis.

IV. DISCUSSION

This implemented method overcomes the conflict between efficiency and resolution in the mechanical scanning near-field measurement method. The 100×100 points near-field distribution and the transformed far-field pattern of the antenna can be accomplished in 5 s, as exhibited in the supplementary video. In contrast, the sampling time of the typical mechanical scanning measurement system is limited by the motor, and a scan of 100×100 points takes about tens of minutes to several hours [46], [47]. The efficiency of this method has a distinct

advantage over existing mechanical scanning methods. The imaging area is temporarily limited by the size of the silicon wafer and is expected to be expanded by simply splicing wafer pieces together.

Although the multilayer matching method reduces the multireflection disturbance and improves the imaging quality, limited by the SNR of the current prototype, the dynamic range in the near-field measurement of Fig. 5 is about 20 dB. This dynamic range is not wide enough for more accurate details of the far-field transformation from the near-field, which is usually recommended to be higher than 30 dB, thus resulting in the truncation of the antenna energy in near-field distribution and affecting the accuracy of the side lobes in the far-field patterns.

The factors affecting current SNR include the limited maximum output power of the VNA, which is 20 dBm and limits the amplitude of the scattering signals. A separately designed transceiver with higher output power and SNR would effectively improve the performance of the method. At the cost of a slightly longer measurement time, it is also feasible to take the average value of multiple measurements or reduce the IF bandwidth of the receiver in VNA to improve the SNR. In addition, reflected or scattered waves from the surrounding environment may produce undesired interference. A cavity covered with absorbing materials is useful to absorb the transmitted waves from the wafer and improve the image quality.

V. CONCLUSION

In this article, a high-efficiency diagnostic approach for the antenna characteristics is realized based on SOPS technology. Several issues limit the application of this efficient imaging method in antenna diagnosis, including the nonnegligible influence of the wafer on the field and small SNR. Multilayer matching is applied to avoid the issue of the multireflection disturbance between the wafer and antenna aperture, which improves the accuracy and SNR of the measurement and enables the method to support more types of AUTs and diagnostic scenarios. A 20 dB Ka-band standard gain antenna is tested as a demonstration, and the diagnostic results of far-field patterns directly transformed from the measured near-field distributions agree well with the simulation results. Diagnosis at an ultraclose distance reveals rare and interesting results. Resonate modes of a handy 2.4 GHz Wi-Fi patch antenna at different radiation states are revealed in the reactive near-field region. In addition, the polarization diagnosis is carried out. With a TM_{01} antenna as the AUT, the full polarization diagnostic ability of the method is verified, and the desired linear polarization component can be selectively imaged with the help of the polarization grid. The systematic diagnoses of antenna radiation characteristics are realized and demonstrated, including near-field distributions, far-field patterns, radiation states in the reactive near-field region, and polarization characteristics. The important thing is that the diagnostic can be taken in seconds. This novel antenna diagnosis method is validated to have wide adaptability, which may open a new avenue of antenna diagnosis and greatly benefit antenna design and optimization.
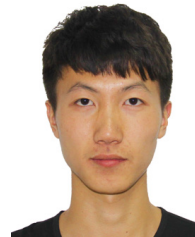
REFERENCES

[1] *IEEE Recommended Practice for Antenna Measurements*, IEEE Standard 149-2021, pp. 1–207, 2022.

[2] A. D. Yaghjian, "An overview of near-field antenna measurements," *IEEE Trans. Antennas Propag.*, vol. AP-34, no. 1, pp. 30–45, Jan. 1986.

[3] *IEEE Recommended Practice for Near-Field Antenna Measurements*, IEEE Standard 1720-2012, pp. 1–102, Dec. 2012.

[4] J. Dyson, "Measurement of near fields of antennas and scatterers," *IEEE Trans. Antennas Propag.*, vol. AP-21, no. 4, pp. 446–460, Jul. 1973.

[5] J.-C. Bolomey et al., "Rapid near-field antenna testing via arrays of modulated scattering probes," *IEEE Trans. Antennas Propag.*, vol. AP-36, no. 6, pp. 804–814, Jun. 1988.

[6] M. Nagai et al., "Generation and detection of terahertz radiation by electro-optical process in GaAs using 1.56 μm fiber laser pulses," *Appl. Phys. Lett.*, vol. 85, no. 18, pp. 3974–3976, Nov. 2004.

[7] B. Yang et al., "Using diamond quantum magnetometer to characterize near-field distribution of patch antenna," *IEEE Trans. Microw. Theory Techn.*, vol. 67, no. 6, pp. 2451–2460, Jun. 2019.

[8] P. Wang et al., "High-resolution vector microwave magnetometry based on solid-state spins in diamond," *Nature Commun.*, vol. 6, no. 1, p. 6631, Mar. 2015.

[9] M. Jing et al., "Atomic superheterodyne receiver based on microwave-dressed Rydberg spectroscopy," *Nature Phys.*, vol. 16, no. 9, pp. 911–915, Sep. 2020.

[10] S. Kumar, H. Fan, H. Kübler, A. J. Jahangiri, and J. P. Shaffer, "Rydberg-atom based radio-frequency electrometry using frequency modulation spectroscopy in room temperature vapor cells," *Opt. Exp.*, vol. 25, no. 8, pp. 8625–8637, Apr. 2017.

[11] G. Giordanengo, M. Righero, F. Vipiana, G. Vecchi, and M. Sabbadini, "Fast antenna testing with reduced near field sampling," *IEEE Trans. Antennas Propag.*, vol. 62, no. 5, pp. 2501–2513, May 2014.

[12] B. Hofmann, O. Neitz, and T. F. Eibert, "On the minimum number of samples for sparse recovery in spherical antenna near-field measurements," *IEEE Trans. Antennas Propag.*, vol. 67, no. 12, pp. 7597–7610, Dec. 2019.

[13] H. Zhao, S. Tao, Z. Chen, and J. Hu, "Sparse source model for prediction of radiations by transmission lines on a ground plane using a small number of near-field samples," *IEEE Antennas Wireless Propag. Lett.*, vol. 18, no. 1, pp. 103–107, Jan. 2019.

[14] R. R. Alavi, R. Mirzavand, J. Doucette, and P. Mousavi, "An adaptive data acquisition and clustering technique to enhance the speed of spherical near-field antenna measurements," *IEEE Antennas Wireless Propag. Lett.*, vol. 18, no. 11, pp. 2325–2329, Nov. 2019.

[15] M. D. Migliore, "A simple introduction to compressed sensing/sparse recovery with applications in antenna measurements," *IEEE Antennas Propag. Mag.*, vol. 56, no. 2, pp. 14–26, Apr. 2014.

[16] M. D. Migliore, "A compressed sensing approach for array diagnosis from a small set of near-field measurements," *IEEE Trans. Antennas Propag.*, vol. 59, no. 6, pp. 2127–2133, Jun. 2011.

[17] S. F. Gregson, Z. Qin, and C. G. Parini, "Compressive sensing in massive MIMO array testing: A practical guide," *IEEE Trans. Antennas Propag.*, vol. 70, no. 9, pp. 7978–7988, Sep. 2022.

[18] G. Oliveri, P. Rocca, and A. Massa, "Reliable diagnosis of large linear arrays—A Bayesian compressive sensing approach," *IEEE Trans. Antennas Propag.*, vol. 60, no. 10, pp. 4627–4636, Oct. 2012.

[19] R. R. Alavi, R. Mirzavand, A. Kiaee, and P. Mousavi, "An adaptive data acquisition technique to enhance the speed of near-field antenna measurement," *IEEE Trans. Antennas Propag.*, vol. 70, no. 7, pp. 5873–5883, Jul. 2022.

[20] M. A. Qureshi, C. H. Schmidt, and T. F. Eibert, "Efficient near-field far-field transformation for nonredundant sampling representation on arbitrary surfaces in near-field antenna measurements," *IEEE Trans. Antennas Propag.*, vol. 61, no. 4, pp. 2025–2033, Apr. 2013.

[21] F. D'Agostino, F. Ferrara, C. Gennarelli, R. Guerriero, and M. Migliozzi, "Nonredundant NF-FF transformation with bi-polar scanning: Experimental testing," in *Proc. AMTA*, Oct. 2016, pp. 1–6.

[22] P. Petre and T. K. Sarkar, "Planar near-field to far-field transformation using an array of dipole probes," *IEEE Trans. Antennas Propag.*, vol. 42, no. 4, pp. 534–537, Apr. 1994.

[23] M. T. Ghasr, M. A. Abou-Khousa, S. Kharkovsky, R. Zoughi, and D. Pommerenke, "Portable real-time microwave camera at 24 GHz," *IEEE Trans. Antennas Propag.*, vol. 60, no. 2, pp. 1114–1125, Feb. 2012.

[24] A. Kiaee, R. R. Alavi, R. Mirzavand, and P. Mousavi, "Numerical and experimental assessment of source reconstruction for very near-field measurements with an array of H-field probes," *IEEE Trans. Antennas Propag.*, vol. 66, no. 3, pp. 1311–1320, Mar. 2018.

[25] M. Tsuchiya, S. Takata, K. Ohsone, S. Fukui, and M. Yorinaga, "Nanoscopic live electrooptic imaging," *Sci. Rep.*, vol. 11, no. 1, p. 5541, Mar. 2021.

[26] B. Yang, Y. Dong, Z.-Z. Hu, G.-Q. Liu, Y.-J. Wang, and G.-X. Du, "Noninvasive imaging method of microwave near field based on solid-state quantum sensing," *IEEE Trans. Microw. Theory Tech.*, vol. 66, no. 5, pp. 2276–2283, May 2018.

[27] L. Ma, N. Leng, M. Jin, and M. Bai, "Real-time imaging of electromagnetic fields," *Opt. Exp.*, vol. 30, no. 12, pp. 20431–20440, Jun. 2022.

[28] W. Platte, "Optoelectronic microwave switching via laser-induced plasma tapers in GaAs microstrip sections," *IEEE Trans. Microw. Theory Techn.*, vol. MTT-29, no. 10, pp. 1010–1018, Oct. 1981.

[29] B. Boyer, J. Haidar, A. Vilcot, and M. Bouthinon, "Tunable microwave load based on biased photoinduced plasma in silicon," *IEEE Trans. Microw. Theory Techn.*, vol. 45, no. 8, pp. 1362–1367, Aug. 1997.

[30] C. D. Gamlath, D. M. Benton, and M. J. Cryan, "Microwave properties of an inhomogeneous optically illuminated plasma in a microstrip gap," *IEEE Trans. Microw. Theory Techn.*, vol. 63, no. 2, pp. 374–383, Feb. 2015.

[31] W. Platte, "Spectral dependence of light-induced microwave reflection coefficient from optoelectronic waveguide gratings," *IEEE Trans. Microw. Theory Techn.*, vol. 43, no. 1, pp. 106–111, Jan. 1995.

[32] A. J. Seeds and A. A. A. De Salles, "Optical control of microwave semiconductor devices," *IEEE Trans. Microw. Theory Techn.*, vol. 38, no. 5, pp. 577–585, May 1990.

[33] L. Ma, N. Leng, X. Z. Ye, M. Jin, and M. Bai, "The distribution measurement of the photo-induced plasma in semiconductor by near-field scanning microwave microscopy," in *Proc. Photon. Electromagn. Res. Symp.-Fall*, Xiamen, China, Dec. 2019, pp. 169–172.

[34] R. Justice and V. H. Rumsey, "Measurement of electric field distributions," *IRE Trans. Antennas Propag.*, vol. 3, no. 4, pp. 177–180, Oct. 1955.

[35] J. Richmond, "A modulated scattering technique for measurement of field distributions," *IRE Trans. Microw. Theory Techn.*, vol. 3, no. 4, pp. 13–15, Jul. 1955.

[36] A. L. Cullen and J. C. Parr, "A new perturbation method for measuring microwave fields in free space," *Proc. IEE-B, Radio Electron. Eng.*, vol. 102, no. 6, pp. 836–844, Nov. 1955.

[37] W. Liang, G. Hygate, J. F. Nye, D. G. Gentle, and R. J. Cook, "A probe for making near-field measurements with minimal disturbance: The optically modulated scatterer," *IEEE Trans. Antennas Propag.*, vol. 45, no. 5, pp. 772–780, May 1997.

[38] W. A. Vitale et al., "Modulated scattering technique in the terahertz domain enabled by current actuated vanadium dioxide switches," *Sci. Rep.*, vol. 7, no. 1, p. 41546, Feb. 2017.

[39] G. Hygate and J. F. Nye, "Measuring microwave fields directly with an optically modulated scatterer," *Meas. Sci. Technol.*, vol. 1, no. 8, pp. 703–709, Aug. 1990.

[40] S. J. Orfanidis, *Electromagnetic Waves and Antennas*. 2016, pp. 153–178 and 800–813. [Online]. Available: https://www.ece.rutgers.edu/~orfanidi/ewa/

[41] R. F. Harrington and J. R. Mautz, "Theory of characteristic modes for conducting bodies," *IEEE Trans. Antennas Propag.*, vol. AP-19, no. 5, pp. 622–628, Sep. 1971.

[42] Y.-L. Kuo and K.-L. Wong, "Printed double-T monopole antenna for 2.4/5.2 GHz dual-band WLAN operations," *IEEE Trans. Antennas Propag.*, vol. 51, no. 9, pp. 2187–2192, Sep. 2003.

[43] M. Cabedo-Fabres, E. Antonino-Daviu, A. Valero-Nogueira, and M. F. Batalle, "The theory of characteristic modes revisited: A contribution to the design of antennas for modern applications," *IEEE Antennas Propag. Mag.*, vol. 49, no. 5, pp. 52–68, Oct. 2007.

[44] S. Kaffash, R. Faraji-Dana, M. Shahabadi, and S. Safavi-Naeini, "A fast computational method for characteristic modes and eigenvalues of array antennas," *IEEE Trans. Antennas Propag.*, vol. 68, no. 12, pp. 7879–7892, Dec. 2020.

[45] C. Fernandes, V. Brankovic, S. Zimmermann, M. Filipe, and L. Anunciada, "Dielectric lens antennas for wireless broadband communications," *Wireless Pers. Commun.*, vol. 10, no. 1, pp. 19–32, Jun. 1999.

[46] S. Hisatake et al., "Near-field measurement and far-field characterization of a J-band antenna based on an electro-optic sensing," in *Proc. 14th Eur. Conf. Antennas Propag. (EuCAP)*, Mar. 2020, pp. 1–4.

[47] G. Alvarez-Narciandi, J. Laviada, Y. Alvarez-Lopez, and F. Las-Heras, "Portable freehand system for real-time antenna diagnosis and characterization," *IEEE Trans. Antennas Propag.*, vol. 68, no. 7, pp. 5636–5645, Jul. 2020.

Liao Ma received the B.S. and M.S. degrees from the School of Electronic and Information Engineering, Beihang University, Beijing, China, in 2008 and 2011, respectively, where he is currently pursuing the Ph.D. degree.

From 2011 to 2018, he worked at Wu Zhong Office of the China Banking and Insurance Regulatory Commission (CBIRC), Beijing, and Ningxia Development and Reform Commission (NXDRC), Ningxia, China. He got a Senior Engineer qualification in 2013. His current research interests include electromagnetic measurement and optic-electric imaging of electromagnetic fields.

Ning Leng received the B.S. and M.S. degrees from Beihang University (BUAA), Beijing, China, in 2018 and 2021, respectively, where he is currently pursuing the Ph.D. degree with the Microwave Engineering Laboratory.

His research interests include near-field scanning microwave microscopy and permittivity measurement.
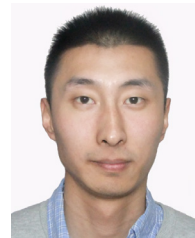
Ming Jin (Member, IEEE) received the B.Sc. and Ph.D. degrees from Beihang University (BUAA), Beijing, China, in 2007 and 2013, respectively.

From 2007 to 2012, he was a Research Assistant with the Microwave Engineering Laboratory, Beihang University. From December 2010 to March 2011, he was a Visiting Scholar with Arizona State University, Tempe, AZ, USA. In 2019, he joined the College of Information Science and Technology, Beijing University of Chemical Technology (BUCT), Beijing, as an Associate Professor. His research interests include microwave radiometer calibration techniques, quasi-optical beam propagation, and computational electromagnetics.

Ming Bai (Member, IEEE) received the B.Sc. and Ph.D. degrees from the Physics Department, University of Science and Technology of China (USTC), Hefei, China, in 1996 and 2002, respectively.

From 2002 to 2006, he worked as a Post-Doctoral Researcher in Technology, with LFSP, Spanish National Research Council (CSIC), Madrid, Spain. He joined Beihang University (BUAA), Beijing, China, in 2006, where he currently working as a Professor with the Microwave Engineering Laboratory. His research interests include computational electromagnetic and microwave imaging.